

Application of the mixed time-averaging semiclassical initial value representation method to complex molecular spectra

Max Buchholz, Frank Grossmann, and Michele Ceotto

Citation: *The Journal of Chemical Physics* **147**, 164110 (2017);

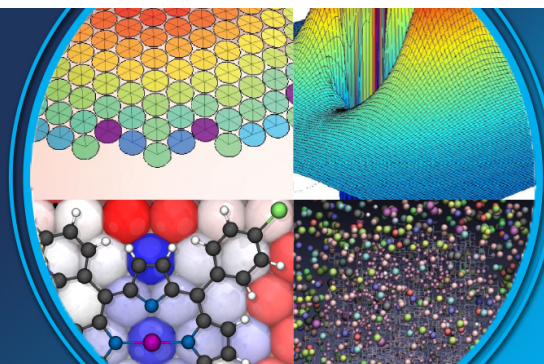
View online: <https://doi.org/10.1063/1.4998510>

View Table of Contents: <http://aip.scitation.org/toc/jcp/147/16>

Published by the *American Institute of Physics*

AIP | The Journal of
Chemical Physics

PERSPECTIVES



Application of the mixed time-averaging semiclassical initial value representation method to complex molecular spectra

Max Buchholz,^{1,2} Frank Grossmann,¹ and Michele Ceotto²

¹*Institut für Theoretische Physik, Technische Universität Dresden, 01062 Dresden, Germany*

²*Dipartimento di Chimica, Università degli Studi di Milano, Via C. Golgi 19, 20133 Milano, Italy*

(Received 1 August 2017; accepted 9 October 2017; published online 26 October 2017)

The recently introduced mixed time-averaging semiclassical initial value representation of the molecular dynamics method for spectroscopic calculations [M. Buchholz, F. Grossmann, and M. Ceotto, *J. Chem. Phys.* **144**, 094102 (2016)] is applied to systems with up to 61 dimensions, ruled by a condensed phase Caldeira-Leggett model potential. By calculating the ground state as well as the first few excited states of the system Morse oscillator, changes of both the harmonic frequency and the anharmonicity are determined. The method faithfully reproduces blueshift and redshift effects and the importance of the counter term, as previously suggested by other methods. Different from previous methods, the present semiclassical method does not take advantage of the specific form of the potential and it can represent a practical tool that opens the route to direct *ab initio* semiclassical simulation of condensed phase systems. *Published by AIP Publishing.* <https://doi.org/10.1063/1.4998510>

I. INTRODUCTION

In a recent publication,¹ it has been shown that the ideas of time-averaging^{2,3} and of semiclassical hybrid dynamics⁴ can be combined and can lead to an accurate description of molecular spectra of an anharmonic system of interest in the presence of an environment. In the present work, the performance of the methodology is tested on systems with a much larger total number of degrees of freedom (DOFs) than treated before, and we specifically answer the question under which condition a redshift or a blueshift of the spectral line of the anharmonic system oscillator is to be expected.

To this end, we employ a time-dependent approach to spectroscopy, pioneered by Heller,⁵ based on the so-called semiclassical initial value representation (SC-IVR) molecular dynamics introduced by Miller.^{6–12} Ignited by the seminal work of Kay in the early 1990s,^{13–15} the literature has recently seen a flurry of activities in SC-IVRs, and the Herman-Kluk (HK) approximation^{10,16} has turned out to be the semiclassical method of choice of many authors.^{17–55} More recently, semiclassical molecular dynamics has been implemented for on-the-fly simulations employing *ab initio* molecular dynamics tools.^{53,56–66}

The HK SC-IVR can, however, be only applied to a relatively small number of coupled degrees of freedom. One route towards the description of the spectra of larger systems is the addition of a time-averaging filter to the phase space integration.^{3,67} When the filter is fully exploited by taking long time-evolved classical trajectories, the phase space integration numerical effort is reduced by an order of magnitude. Further improvement in computational cost to just a handful of classical trajectories is achieved by taking into consideration that accurate eigenvalues can be obtained from single trajectories when these are close in energy to the

eigenvalues. In fact, the trajectories whose energies are about the same as the vibrational peaks' energies are contributing most to the spectroscopic signal. This approach is called Multiple Coherent TA-SCIVR (MC-SCIVR or MC-TA-SCIVR) and it has proved to be accurate for molecules such as H₂O, CH₄, CH₂D₂, and NH₃.^{56,60,68,69} The significant reduction in the number of classical trajectories offered by the MC-TA-SCIVR approach allowed us to obtain quite accurate power spectra of molecules using a direct *ab initio* dynamics simulation, also called on-the-fly or direct *ab initio* semiclassical dynamics.^{56–60,68–72} More recently, to beat the curse of dimensionality, a projection technique has been introduced. The new method is called Divide-and-Conquer SCIVR (DC SCIVR) and it allows the calculation of power spectra for high dimensional systems, such as a fullerene buckyball molecule.⁷³

An alternative approach to reduce the number of classical trajectories is Heller's thawed Gaussian wavepacket dynamics (TGWD),⁷ where only a single Gaussian wavepacket with time-dependent width is propagated. This numerically very cheap method is accurate only for at most harmonic potentials, but it can be combined with the more demanding HK method in the semiclassical hybrid dynamics formalism.⁴ Propagating only few degrees of freedom on the HK level, while using the simpler TGWD for the larger environmental part, gives rise to an accurate yet efficient description for the dynamics of systems with many degrees of freedom. We have recently combined the hybrid idea with the time-averaging filter to arrive at the mixed TA-SCIVR method (M-TA-SCIVR) that needs fewer trajectories for convergence than a full TA-SCIVR treatment while being just as accurate for the HK degrees of freedom.¹

A model system that allows for an easy distinction of degrees of freedom to be treated on the HK versus TGWD level is the one used by Caldeira and Leggett (CL) in their

seminal path integral studies of quantum dissipation.⁷⁴ This model with different analytical forms of spectral density and cutoff has been widely used in different branches of the quantum dynamics community to model system-bath interactions.^{22,75–81} Using a normal mode analysis, Pollak and co-workers have analytically shown for a harmonic system with and without an additional cubic term that the system frequency shift induced by the CL bath with an Ohmic spectral density is always towards higher frequencies, i.e., a blueshift.^{75,82} For the cubic system, another analytical study has also shown a blueshift tendency for different bath spectral densities.⁸³ The same result has been obtained for a Morse oscillator coupled to a CL bath.⁸⁴ On the other hand, arguing that experimental results often report a redshift of the system frequency (for example, for iodine in rare gas matrices^{85,86}), Georgievskii and Stuchebrukhov⁸⁷ have investigated the influence of the CL counter term on a cubic system potential and found that by omitting the counter term, both blueshift and redshift are possible depending on bath parameters. We will employ a discretized Ohmic spectral density, frequently applied in the CL model, and explicitly treat the dynamics of the combined system, comprising the anharmonic system of interest as well as the bilinearly coupled harmonic bath modes. For up to ten bath degrees of freedom, this can still be done on the Herman-Kluk level of the semiclassical description and serves as a benchmark for our more approximate M-TA-SCIVR method that has to be used if up to 60 bath degrees of freedom are taking part in the dynamics. Studying both cases of a non-resonant and a resonant bath, we will show that both redshifts and blueshifts are observed.

This paper is organized in the following way: Sec. II recalls the mixed time-averaging semiclassical method for the calculation of molecular spectra. In Sec. III, we recapitulate the CL model and discuss the discretization of the bath's spectral density. In Sec. IV results are first given for ten bath oscillators and different levels of approximation. The high quality of the results of our proposed approximation methodology is thereby shown. Then a detailed study of the frequency shift of the oscillator of interest in the presence of a substantial number of bath degrees of freedom is performed. Conclusions are drawn and an outlook is given in Sec. V.

II. MIXED TIME-AVERAGING SEMICLASSICAL INITIAL VALUE REPRESENTATION

We first recapitulate the mixed time-averaging semiclassical initial value approach to the calculation of molecular spectra. This method has been introduced recently¹ and it combines the semiclassical hybrid dynamics⁴ with time-averaging.^{2,3}

The goal of the method is to calculate the power spectrum $I(E)$ of a given initial state $|\chi\rangle$ subject to a Hamiltonian \hat{H} ,

$$I(E) = \sum_n |\langle \chi | \psi_n \rangle|^2 \delta(E - E_n), \quad (1)$$

where E_n are the eigenenergies of interest and $|\psi_n\rangle$ are the corresponding eigenfunctions of \hat{H} . The spectrum can be found

from the system's dynamics by expressing the delta function as a Fourier integral. Equation (1) then becomes

$$I(E) = \frac{1}{2\pi\hbar} \int_{-\infty}^{\infty} dt e^{iEt/\hbar} \langle \chi | e^{-i\hat{H}t/\hbar} | \chi \rangle. \quad (2)$$

The time evolution in Eq. (2) is calculated semiclassically with the propagator by Herman and Kluk,¹⁰

$$e^{-i\hat{H}t/\hbar} = \frac{1}{(2\pi\hbar)^F} \int d\mathbf{p}(0) \int d\mathbf{q}(0) C_t(\mathbf{p}(0), \mathbf{q}(0)) e^{iS_t(\mathbf{p}(0), \mathbf{q}(0))/\hbar} \times |\mathbf{p}(t), \mathbf{q}(t)\rangle \langle \mathbf{p}(0), \mathbf{q}(0)|, \quad (3)$$

where $(\mathbf{p}(t), \mathbf{q}(t))$ is the $2F$ -dimensional classical trajectory evolving from initial conditions $(\mathbf{p}(0), \mathbf{q}(0))$, and S_t is the corresponding classical action. Equation (3) also contains the HK prefactor,

$$C_t(\mathbf{p}(0), \mathbf{q}(0)) = \sqrt{\frac{1}{2^F} \det \left[\frac{\partial \mathbf{q}(t)}{\partial \mathbf{q}(0)} + \frac{\partial \mathbf{p}(t)}{\partial \mathbf{p}(0)} - i\hbar \gamma \frac{\partial \mathbf{q}(t)}{\partial \mathbf{p}(0)} + \frac{i}{\hbar \gamma} \frac{\partial \mathbf{p}(t)}{\partial \mathbf{q}(0)} \right]}, \quad (4)$$

which accounts for second-order quantum delocalizations around the classical paths. Finally, the coherent state basis set in position representation for many degrees of freedom is given by the direct product of one-dimensional coherent states,

$$\langle \mathbf{x} | \mathbf{p}, \mathbf{q} \rangle = \left(\frac{\det(\gamma)}{\pi^F} \right)^{1/4} \times \exp \left[-\frac{1}{2} (\mathbf{x} - \mathbf{q})^T \gamma (\mathbf{x} - \mathbf{q}) + \frac{i}{\hbar} \mathbf{p}^T (\mathbf{x} - \mathbf{q}) \right], \quad (5)$$

where γ is a diagonal matrix containing F time independent width parameters.

While the semiclassical approximation of the propagator in Eq. (3) in principle allows for the inclusion of an arbitrary number of DOFs, practical applications are limited by the need to converge the phase space integral. Therefore, we will now present two methods that are aimed at accelerating the numerical Monte Carlo phase space integration of Eq. (3). The first step is the introduction of a time-averaging integral,^{2,3} which is applied to Eq. (2) and yields a semiclassical approximation with a pre-averaged phase space integrand,

$$I(E) = \frac{1}{(2\pi\hbar)^F} \int d\mathbf{p}(0) \int d\mathbf{q}(0) \frac{1}{\pi\hbar T} \text{Re} \int_0^T dt_1 \times \int_{t_1}^T dt_2 C_{t_2}(\mathbf{p}(t_1), \mathbf{q}(t_1)) \times \langle \chi | \mathbf{p}(t_2), \mathbf{q}(t_2) \rangle e^{i[S_2(\mathbf{p}(0), \mathbf{q}(0)) + Et_2]/\hbar} \times \left[\langle \chi | \mathbf{p}(t_1), \mathbf{q}(t_1) \rangle e^{i[S_1(\mathbf{p}(0), \mathbf{q}(0)) + Et_1]/\hbar} \right]^*. \quad (6)$$

In order to recover a single time integration as in Eq. (2), Kaledin and Miller have suggested the so-called separable

approximation,³ where the prefactor is written as $C_{t_2}(\mathbf{p}(t_1), \mathbf{q}(t_1)) \approx \exp[i(\phi(t_2) - \phi(t_1))/\hbar]$, and $\phi(t)/\hbar = \text{phase}[C_t(\mathbf{p}(0), \mathbf{q}(0))]$. This procedure is exact in the harmonic limit and results in the expression

$$I(E) = \frac{1}{(2\pi\hbar)^F} \frac{1}{2\pi\hbar T} \int d\mathbf{p}(0) \int d\mathbf{q}(0) \left| \int_0^T dt \langle \chi | \mathbf{p}(t), \mathbf{q}(t) \rangle \right|^2 \times e^{i[S_t(\mathbf{p}(0), \mathbf{q}(0)) + Et + \phi_t(\mathbf{p}(0), \mathbf{q}(0))]/\hbar}, \quad (7)$$

which contains only a single and positive-definite phase space integrand that is expected to be more stable numerically than the two-time integration in Eq. (6). While clearly less computationally demanding than Eq. (6), the separable approximation in Eq. (7) has also turned out to be very accurate for a number of molecular dynamics applications.^{1,3,56–60,67–72,88}

The second step towards making the dynamics of larger systems accessible is to invoke the mixed approximation. To this end, we use the semiclassical hybrid dynamics idea to divide the $2F$ phase space variables into $2F_{\text{hk}}$ for the system space and $2F_{\text{tg}}$ for the bath phase space. Only the system part, denoted by the subscript hk, is then treated on the HK level of accuracy, whereas the simpler single-trajectory TGWD approximation is used for the bath DOFs, which are denoted by the subscript tg. This separation is made only for the semiclassical expression, while the underlying classical dynamics is not modified. We now assume a reference state of Gaussian form, $|\chi\rangle = |\mathbf{p}_{\text{eq}}, \mathbf{q}_{\text{eq}}\rangle$, where \mathbf{q}_{eq} is the equilibrium position and \mathbf{p}_{eq} is the momentum corresponding to some eigenenergy. In the mixed approximation, the initial phase space coordinates are

$$\mathbf{p}_{\text{eq}}(0) = \begin{pmatrix} \mathbf{p}_{\text{hk}}(0) \\ \mathbf{p}_{\text{eq, tg}}(0) \end{pmatrix}, \quad \mathbf{q}_{\text{eq}}(0) = \begin{pmatrix} \mathbf{q}_{\text{hk}}(0) \\ \mathbf{q}_{\text{eq, tg}}(0) \end{pmatrix}. \quad (8)$$

Only the HK initial conditions $(\mathbf{p}_{\text{hk}}(0), \mathbf{q}_{\text{hk}}(0))$ are found by Monte Carlo sampling around $(\mathbf{p}_{\text{eq, hk}}, \mathbf{q}_{\text{eq, hk}})$, while the bath starting coordinates are always at the equilibrium positions, $(\mathbf{p}_{\text{eq, tg}}(0), \mathbf{q}_{\text{eq, tg}}(0)) = (\mathbf{p}_{\text{eq, tg}}, \mathbf{q}_{\text{eq, tg}})$. Since the TGWD is exact for harmonic potentials, this division should accurately reproduce the contributions of weakly coupled bath DOFs

close to their potential minimum. With this separation in place, we expand the classical trajectories and the action to first and second order, respectively, in the displacement coordinates of the bath subspace,

$$\delta\mathbf{p}_{\text{tg}} = \mathbf{p}_{\text{tg}}(0) - \mathbf{p}_{\text{eq, tg}}(0), \quad \delta\mathbf{q}_{\text{tg}} = \mathbf{q}_{\text{tg}}(0) - \mathbf{q}_{\text{eq, tg}}(0). \quad (9)$$

This approximates the exponent in Eq. (7) such that the phase space integration over the original bath initial conditions $(\mathbf{p}_{\text{tg}}(0), \mathbf{q}_{\text{tg}}(0))$ can be performed analytically as a Gaussian integral. The expanded classical trajectories becomes

$$\mathbf{p}(t) = \begin{pmatrix} \mathbf{p}_{\text{hk}}(t) \\ \mathbf{p}_{\text{tg}}(t) \end{pmatrix} = \mathbf{p}_{\text{eq}}(t) + \mathbf{m}_{11}(t)\delta\mathbf{p}_{\text{tg}} + \mathbf{m}_{12}(t)\delta\mathbf{q}_{\text{tg}}, \quad (10)$$

$$\mathbf{q}(t) = \begin{pmatrix} \mathbf{q}_{\text{hk}}(t) \\ \mathbf{q}_{\text{tg}}(t) \end{pmatrix} = \mathbf{q}_{\text{eq}}(t) + \mathbf{m}_{21}(t)\delta\mathbf{p}_{\text{tg}} + \mathbf{m}_{22}(t)\delta\mathbf{q}_{\text{tg}},$$

and the action is

$$\begin{aligned} S_t(\mathbf{p}(0), \mathbf{q}(0)) &= S_t(\mathbf{p}_{\text{hk}}(0), \mathbf{q}_{\text{hk}}(0), \mathbf{p}_{\text{eq, tg}}(0), \mathbf{q}_{\text{eq, tg}}(0)) \\ &+ \mathbf{p}_{\text{eq}}^T(t) \mathbf{m}_{21}(t) \delta\mathbf{p}_{\text{tg}} + (\mathbf{p}_{\text{eq}}^T(t) \mathbf{m}_{22}(t) - \mathbf{p}_{\text{eq, 0, tg}}^T) \delta\mathbf{q}_{\text{tg}} \\ &+ \frac{1}{2} \delta\mathbf{p}_{\text{tg}}^T \mathbf{m}_{11}^T(t) \mathbf{m}_{21}(t) \delta\mathbf{p}_{\text{tg}} + \frac{1}{2} \delta\mathbf{q}_{\text{tg}}^T \mathbf{m}_{12}^T(t) \mathbf{m}_{22}(t) \delta\mathbf{q}_{\text{tg}} \\ &+ \delta\mathbf{q}_{\text{tg}}^T \mathbf{m}_{12}^T(t) \mathbf{m}_{21}(t) \delta\mathbf{p}_{\text{tg}}. \end{aligned} \quad (11)$$

\mathbf{m}_{ij} in Eqs. (10) and (11) are non-square $F \times F_{\text{tg}}$ submatrices of the stability matrix,

$$\begin{aligned} \mathbf{m}_{11}(t) &= \frac{\partial \mathbf{p}_{\text{eq}}(t)}{\partial \mathbf{p}_{\text{eq, tg}}(0)}, & \mathbf{m}_{12}(t) &= \frac{\partial \mathbf{p}_{\text{eq}}(t)}{\partial \mathbf{q}_{\text{eq, tg}}(0)}, \\ \mathbf{m}_{21}(t) &= \frac{\partial \mathbf{q}_{\text{eq}}(t)}{\partial \mathbf{p}_{\text{eq, tg}}(0)}, & \mathbf{m}_{22}(t) &= \frac{\partial \mathbf{q}_{\text{eq}}(t)}{\partial \mathbf{q}_{\text{eq, tg}}(0)}. \end{aligned} \quad (12)$$

They will be used only for the TG part of the mixed TA-SCIVR integrand, while the phase ϕ_t of the HK prefactor still comprises the full $F \times F$ matrices from Eq. (4). After unraveling the modulus in Eq. (7) and inserting Eqs. (10) and (11), the phase space integration over the TG DOFs can be performed analytically as a Gaussian integral. This results in the mixed TA-SCIVR expression

$$\begin{aligned} I(E) &= \frac{1}{(2\hbar)^F} \frac{1}{\pi^{F_{\text{hk}}}} \frac{\text{Re}}{\pi\hbar T} \int d\mathbf{p}_{\text{hk}}(0) \int d\mathbf{q}_{\text{hk}}(0) \int_0^T dt_1 \int_{t_1}^T dt_2 \\ &\times e^{i[E(t_1 - t_2) + \phi_{t_1}(\mathbf{p}_{\text{eq}}(0), \mathbf{q}_{\text{eq}}(0)) - \phi_{t_2}(\mathbf{p}_{\text{eq}}(0), \mathbf{q}_{\text{eq}}(0)) + S_{t_1}(\mathbf{p}_{\text{eq}}(0), \mathbf{q}_{\text{eq}}(0)) - S_{t_2}(\mathbf{p}_{\text{eq}}(0), \mathbf{q}_{\text{eq}}(0))]/\hbar} \\ &\times \langle \mathbf{p}_{\text{eq, hk}}, \mathbf{q}_{\text{eq, hk}} | \mathbf{p}_{\text{eq, hk}}(t_1), \mathbf{q}_{\text{eq, hk}}(t_1) \rangle \langle \mathbf{p}_{\text{eq, hk}}(t_2), \mathbf{q}_{\text{eq, hk}}(t_2) | \mathbf{p}_{\text{eq, hk}}, \mathbf{q}_{\text{eq, hk}} \rangle \end{aligned} \quad (13)$$

$$\begin{aligned} &\times \sqrt{\frac{1}{\det(\mathbf{A}(t_1) + \mathbf{A}^*(t_2))}} \\ &\times \langle \mathbf{p}_{\text{eq, tg}}, \mathbf{q}_{\text{eq, tg}} | \mathbf{p}_{\text{eq, tg}}(t_1), \mathbf{q}_{\text{eq, tg}}(t_1) \rangle \langle \mathbf{p}_{\text{eq, tg}}(t_2), \mathbf{q}_{\text{eq, tg}}(t_2) | \mathbf{p}_{\text{eq, tg}}, \mathbf{q}_{\text{eq, tg}} \rangle \\ &\times \exp \left\{ \frac{1}{4} (\mathbf{b}_{t_1} + \mathbf{b}_{t_2}^*)^T (\mathbf{A}(t_1) + \mathbf{A}^*(t_2))^{-1} (\mathbf{b}_{t_1} + \mathbf{b}_{t_2}^*) \right\}, \end{aligned} \quad (14)$$

which contains some newly defined expressions, namely, the symmetric $2F_{\text{tg}} \times 2F_{\text{tg}}$ matrix $\mathbf{A}(t)$ with blocks

$$\begin{aligned}
\mathbf{A}_{11}(t) &= \frac{1}{4} \mathbf{m}_{21}^T(t) \boldsymbol{\gamma} \mathbf{m}_{21}(t) + \frac{1}{4\hbar^2} \mathbf{m}_{11}^T(t) \boldsymbol{\gamma}^{-1} \mathbf{m}_{11}(t), \\
\mathbf{A}_{12}(t) &= \frac{1}{4} \mathbf{m}_{21}^T(t) \boldsymbol{\gamma} \mathbf{m}_{22}(t) + \frac{1}{4\hbar^2} \mathbf{m}_{11}^T(t) \boldsymbol{\gamma}^{-1} \mathbf{m}_{12}(t), \\
\mathbf{A}_{21}(t) &= \frac{1}{4} \mathbf{m}_{22}^T(t) \boldsymbol{\gamma} \mathbf{m}_{21}(t) + \frac{1}{4\hbar^2} \mathbf{m}_{12}^T(t) \boldsymbol{\gamma}^{-1} \mathbf{m}_{11}(t), \\
\mathbf{A}_{22}(t) &= \frac{1}{4} \mathbf{m}_{22}^T(t) \boldsymbol{\gamma} \mathbf{m}_{22}(t) + \frac{1}{4\hbar^2} \mathbf{m}_{12}^T(t) \boldsymbol{\gamma}^{-1} \mathbf{m}_{12}(t)
\end{aligned} \quad (15)$$

and the $2F_{\text{tg}}$ -dimensional vector $\mathbf{b}(t) \equiv (\mathbf{b}_{1,t}^T, \mathbf{b}_{2,t}^T)^T$ with sub-vectors

$$\begin{aligned}
\mathbf{b}_{1,t}^T &= -\frac{1}{2} (\mathbf{q}(t) - \mathbf{q}(0))^T \left[\boldsymbol{\gamma} \mathbf{m}_{21}(t) + \frac{i}{\hbar} \mathbf{m}_{11}(t) \right] \\
&\quad - \frac{1}{2\hbar^2} (\mathbf{p}(t) - \mathbf{p}(0))^T \left[\boldsymbol{\gamma}^{-1} \mathbf{m}_{11}(t) - i\hbar \mathbf{m}_{21}(t) \right], \\
\mathbf{b}_{2,t}^T &= -\frac{1}{2} (\mathbf{q}(t) - \mathbf{q}(0))^T \left[\boldsymbol{\gamma} \mathbf{m}_{22}(t) + \frac{i}{\hbar} \mathbf{m}_{12}(t) \right] \\
&\quad - \frac{1}{2\hbar^2} (\mathbf{p}(t) - \mathbf{p}(0))^T \left[\boldsymbol{\gamma}^{-1} \mathbf{m}_{12}(t) - i\hbar \mathbf{m}_{22}(t) \right].
\end{aligned} \quad (16)$$

The expressions for $\mathbf{A}(t)$ and $\mathbf{b}(t)$ differ from our first publication on this matter,¹ as we have left out two constant imaginary contributions in Eqs. (15) and (16) that cancel out in the phase space integrand in Eq. (13). Another difference to Ref. 1 is that we have explicitly written out the scalar quantity c_t , which has been defined there and which contained the action as well as the overlap of the TG part with the initial state.

Comparing Eq. (13) to the full HK expressions (6) and (7), we have achieved a reduction in the dimensionality of the phase space that has to be sampled over. The loss in accuracy is expected to be minimal, as the bath DOFs that are treated on the

TG level are weakly coupled and therefore close to harmonic behavior. Again, we stress that there is no decoupling of the underlying classical dynamics.

While the reduced Monte Carlo sampling is clearly advantageous for numerical efficiency, it has come at the price of reintroducing two time integrations in Eq. (13). The integration itself poses no difficulty, as it is simply a two-dimensional Fourier transformation, but calculating the integrand for N_{steps}^2 time steps takes a lot of computational time. Therefore, it is highly desirable to find an expression with only a single time integration. In the spirit of the original separable approximation that leads from Eq. (6) to Eq. (7), we proceed by assuming a form for the TG exponent and the TG prefactor that is exact for the harmonic oscillator.¹ The separable form of the exponent reads as

$$\begin{aligned}
&\frac{1}{4} (\mathbf{b}_{t_1} + \mathbf{b}_{t_2}^*)^T (\mathbf{A}(t_1) + \mathbf{A}^*(t_2))^{-1} (\mathbf{b}_{t_1} + \mathbf{b}_{t_2}^*) \\
&\approx \frac{1}{4} \mathbf{b}_{t_1}^T (\mathbf{A}(t_1) + \mathbf{A}^*(t_1))^{-1} \mathbf{b}_{t_1} \\
&\quad + \frac{1}{4} \left[\mathbf{b}_{t_2}^T (\mathbf{A}(t_2) + \mathbf{A}^*(t_2))^{-1} \mathbf{b}_{t_2} \right]^*, \quad (17)
\end{aligned}$$

and the TG prefactor is separated in the fashion of a geometric average,

$$\begin{aligned}
\frac{1}{\sqrt{\det(\mathbf{A}(t_1) + \mathbf{A}^*(t_2))}} &\approx \left(\frac{1}{\det(\mathbf{A}(t_1) + \mathbf{A}(t_1))} \right)^{1/4} \\
&\quad \times \left(\frac{1}{\det(\mathbf{A}(t_2) + \mathbf{A}(t_2))} \right)^{1/4}. \quad (18)
\end{aligned}$$

With that, we arrive at the desired separable mixed TA-SCIVR

$$\begin{aligned}
I(E) &= \frac{1}{(2\hbar)^F} \frac{1}{\pi^{F_{\text{hk}}}} \frac{1}{2\pi\hbar T} \int d\mathbf{p}_{\text{hk}}(0) \int d\mathbf{q}_{\text{hk}}(0) \left| \int_0^T dt e^{i[Et + \phi_t(\mathbf{p}_{\text{eq}}(0), \mathbf{q}_{\text{eq}}(0)) + S_t(\mathbf{p}_{\text{eq}}(0), \mathbf{q}_{\text{eq}}(0))]/\hbar} \right. \\
&\quad \times \langle \mathbf{p}_{\text{eq, hk}}, \mathbf{q}_{\text{eq, hk}} | \mathbf{p}_{\text{eq, hk}}(t), \mathbf{q}_{\text{eq, hk}}(t) \rangle \langle \mathbf{p}_{\text{eq, tg}}, \mathbf{q}_{\text{eq, tg}} | \mathbf{p}_{\text{eq, tg}}(t), \mathbf{q}_{\text{eq, tg}}(t) \rangle \\
&\quad \times \left. \frac{1}{[\det(\mathbf{A}(t) + \mathbf{A}^*(t))]^{1/4}} \exp \left\{ \frac{1}{4} \mathbf{b}_t^T (\mathbf{A}(t) + \mathbf{A}^*(t))^{-1} \mathbf{b}_t \right\} \right|^2. \quad (19)
\end{aligned}$$

As we have seen for two-dimensional and three-dimensional model systems,¹ this approximation reproduces both system and bath peaks precisely when compared with exact quantum dynamics results and reaches tight convergence within a considerably shorter amount of time than the separable TA-SCIVR from Eq. (7).

In Sec. IV, we show that this high accuracy is also achieved for larger systems, and we then go on to use the mixed approximation to investigate the influence of the Caldeira-Leggett counter term on the frequency shift of an anharmonic Morse system. We note in passing that a linearization along the lines of linearized SC-IVRs (LSC-IVRs) is not possible because we just have a single time-evolution operator in our starting expression (1), while the LSC-IVR is propagating densities.^{26,89-91}

III. MODEL: MORSE OSCILLATOR COUPLED TO A CALDEIRA-LEGGETT BATH

In order to test the accuracy of the mixed TA-SCIVR, we use a Morse oscillator coupled bilinearly to a Caldeira-Leggett (CL) bath of harmonic oscillators. The Hamiltonian in atomic units has the form

$$\begin{aligned}
H &= \frac{p_s^2}{2m_s} + V_s(s) + \sum_{i=1}^{F_b} \left[\frac{p_i^2}{2} + \frac{1}{2} \omega_i^2 y_i^2 + c_i y_i (s - s_{\text{eq}}) \right. \\
&\quad \left. + \frac{1}{2} \frac{c_i^2}{\omega_i^2} (s - s_{\text{eq}})^2 \right], \quad (20)
\end{aligned}$$

where the Morse potential for the system coordinate s is

$$V_s(s) = D_e \left(1 - e^{-\alpha(s - s_{\text{eq}})} \right)^2, \quad (21)$$

and we take the parameters of molecular iodine⁹² for the dissociation energy $D_e = 0.057$ a.u., for the equilibrium distance $s_{\text{eq}} = 5.001$ a.u., and for the range parameter $\alpha = 0.983$ a.u. The reduced mass of the Morse oscillator is $m_s = m_r = 1.165 \times 10^5$ a.u. There is an analytic solution for the eigenenergies of the Morse potential which we will need later for comparison,

$$E_n = \omega_e \left(n + \frac{1}{2} \right) - \omega_e x_e \left(n + \frac{1}{2} \right)^2, \quad (22)$$

where $\omega_e = \alpha / \sqrt{m_r / (2D_e)}$ is the frequency of the harmonic approximation to the Morse potential, and $x_e = \omega_e / (4D_e)$ is the anharmonicity parameter. For the iodine parameters above, these quantities become $\omega_e = 9.724 \times 10^{-4}$ a.u. and $x_e = 4.264 \times 10^{-3}$ a.u.

The bath part of the Hamiltonian in Eq. (20) consists of the bath kinetic energy, the bilinear system-bath coupling, where y_i denotes the bath DOFs, and the Caldeira-Leggett counter term. The latter is introduced in order to prevent a renormalization of the potential,⁹³ and we will look into its influence on the system spectrum in Sec. IV. Following Refs. 20 and 94, we use an Ohmic spectral density with an exponential cutoff,

$$J_e(\omega) = \eta \omega e^{-\omega/\omega_c}, \quad (23)$$

with the system-bath coupling strength η and a cutoff frequency ω_c . In discretized form, the density is defined as

$$J(\omega) = \frac{\pi}{2} \sum_{i=1}^{F_b} \frac{c_i^2}{\omega_i} \delta(\omega - \omega_i), \quad (24)$$

and the coupling coefficients c_i in Eq. (20) are chosen such that it becomes equivalent to the continuous form in the limit of infinitely many bath oscillators,

$$c_i^2 = \frac{2}{\pi} \omega_i \frac{J_e(\omega_i)}{\rho(\omega_i)}, \quad (25)$$

with the frequency density defined by the condition

$$\int_0^{\omega_i} d\omega \rho(\omega) = i \quad \text{for } i = 1, \dots, F_b. \quad (26)$$

Here, we choose it as

$$\rho(\omega) = a \frac{J_e(\omega)}{\omega}, \quad (27)$$

where a is a normalization coefficient to ensure that $i = F_b$ if the largest bath frequency $\omega_i = \omega_{\text{max}}$ is chosen in Eq. (26), and it amounts to

$$a = \frac{F_b}{\eta \omega_c} \frac{1}{1 - e^{-\omega_{\text{max}}/\omega_c}}. \quad (28)$$

With Eqs. (24), (26), and (27), one finds the discrete frequencies as

$$\omega_i = -\omega_c \ln \left(1 - \frac{i(1 - e^{-\omega_{\text{max}}/\omega_c})}{F_b} \right). \quad (29)$$

If both the cutoff frequency and the maximum frequency of the bath are chosen much smaller than the system frequency, about $F_b = 20$ bath oscillators have been shown to be sufficient to reproduce a continuous bath.²⁰ The semiclassical hybrid approach in particular has already turned out to provide an adequate description for the short-time decay of quantum

coherence of this specific system-bath problem.⁹⁴ We also choose this frequency density because it allows setting up a bath containing not only many low-frequency modes but also a few oscillators with frequencies close to the system frequency. A thorough study comparing different spectral densities with their advantages and drawbacks is given in Ref. 95.

IV. RESULTS AND DISCUSSION

The main objective of this paper is the description of the frequency shift of a Morse oscillator coupled to a CL bath using the mixed TA-SCIVR. In order to demonstrate the very good accuracy of the mixed approach, and in particular the separable approximation, we first discuss results for a ten-dimensional bath where TA HK results according to Eq. (7) can still be found relatively easily. After making this comparison, we will turn to baths with up to 60 DOFs and different bath parameters to show their influence on the system spectrum. A specific focus will be on the role of the CL counter term for the anharmonic spectrum.

We employ two different frequency combinations: one with a resonant maximum frequency, $\omega_c = 0.5 \omega_s$ and $\omega_{\text{max}} = \omega_s$, and a low-frequency bath with $\omega_c = 0.1 \omega_s$ and $\omega_{\text{max}} = 0.2 \omega_s$. We choose two different effective coupling parameters $\eta_{\text{eff}} = \eta / (m_s \omega_s)$, namely, $\eta_{\text{eff}} = 0.5$ and $\eta_{\text{eff}} = 2.0$ for the bath with small cutoff frequency and $\eta_{\text{eff}} = 0.1$ and $\eta_{\text{eff}} = 0.5$ for the big cutoff. The center of the initial wavepacket is at equilibrium with nonzero momentum $(0, \sqrt{m_s \omega_s})$ for the system DOF. The centers of the bath oscillators' wavepackets are located at $(0,0)$ because otherwise the spectrum becomes very dense due to the huge number of excited bath peaks (for an example with 19 DOFs, see Fig. 3 of Ref. 71). In general, these simplified initial conditions might not be adequate to describe the system frequency shift because possible anharmonic contributions of the bath DOFs are neglected by a dynamics that mainly explores the harmonic neighborhood of the potential minimum. For the bilinearly coupled, harmonic CL bath, however, the difference in the system frequencies arising from initially excited bath DOFs is negligible. The number of semiclassical time steps is $N_{\text{steps}} = 2^{14}$ and their length is $\Delta t = (2\pi/\omega_e)/20$, resulting in a frequency resolution of 1.2×10^{-6} a.u. (0.55 cm^{-1}).

A. Morse oscillator coupled to ten harmonic oscillators

We first discuss an interesting but relatively simple example: the bath comprising ten oscillators with $\omega_c = 0.5 \omega_s$, $\omega_{\text{max}} = \omega_s$, and $\eta_{\text{eff}} = 0.5$ (Figs. 1 and 2). In Fig. 1, we give an overview of results obtained with the different methods. The degree of approximation always decreases from top to bottom: the separable mixed approximation according to Eq. (19) is indicated with magenta lines, the full mixed approximation Eq. (13) is blue for one and green for two HK DOFs, and the reference separable TA-SCIVR [Eq. (6)] is red. In the full mixed approximation calculations, either only the Morse DOF is treated with HK or both the Morse oscillator and the resonant bath mode are treated with HK, which is expected to experience the strongest anharmonic driving by the system. Only 10^4 trajectories have been used in each case, both to achieve reasonable computational costs and to work out the efficiency

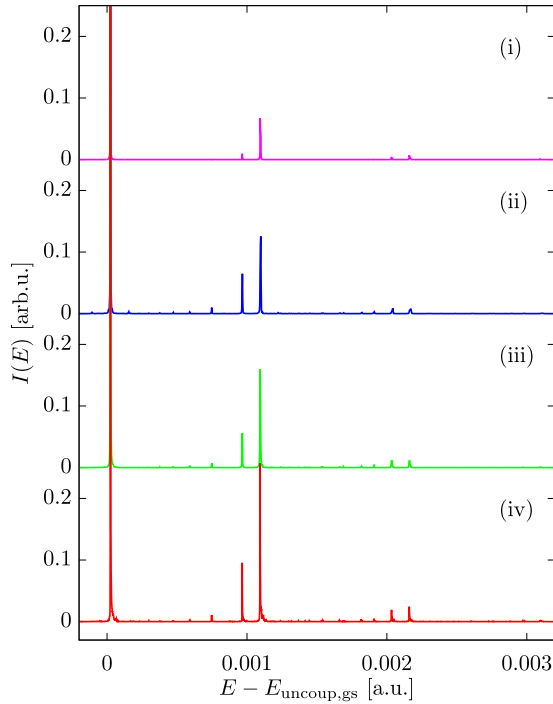


FIG. 1. Spectrum of an iodine-like Morse oscillator coupled to a CL bath comprising 10 DOFs with $\omega_{\max} = \omega_s$, $\omega_c = 0.5 \omega_s$, and coupling $\eta_{\text{eff}} = 0.5$. From top to bottom: separable TA mixed with 1 HK DOF [magenta, (i)] [Eq. (19)], full TA mixed with 1 HK DOF [blue, (ii)] and full TA mixed with 2 HK DOFs [green, (iii)] [Eq. (13)], and the separable TA HK [red, (iv)] using Eq. (6). All spectra are renormalized such that the elastic peak has height one, and all spectra are magnified and overlapped in order to make excited peaks visible.

of the new methods. In all spectral plots, we subtract the sum of the ground state energies of the individual DOFs,

$$E_{\text{plot}} = E - E_0 - \sum_{i=1}^{F_b} \frac{\omega_i}{2}, \quad (30)$$

in order to make the net effect of the system-bath coupling visible and to facilitate the comparison between baths with different parameters. In Eq. (30), E_0 is the ground state energy of the Morse oscillator.

Overall, agreement in terms of peak position is very good between all methods. The peak weights are not reproduced correctly as a consequence of the different degrees of approximation in the mixed treatments. This loss of accuracy in peak weight is, however, inherent also in the reference results obtained with the separable approximation for TA HK when compared to full quantum calculations, as we have seen in Ref. 1 for 2D and 3D examples. We will therefore focus mainly on frequencies in the discussion. Bath peaks are generally not very prominent because there is no initial excitation in the bath; the only dynamics is induced by the system. This is reflected especially in the reference TA-SCIVR and in the full mixed spectra. The biggest bath peaks correspond to the modes whose frequency is closest to the system and which are therefore most strongly driven by the system. By contrast, just one bath peak from the resonant harmonic oscillator (HO) is featured significantly in the separable mixed spectrum [magenta line, (i)].

In Fig. 2, we provide a closer look at one exemplary region of the spectrum. The respective rightmost peak is the second

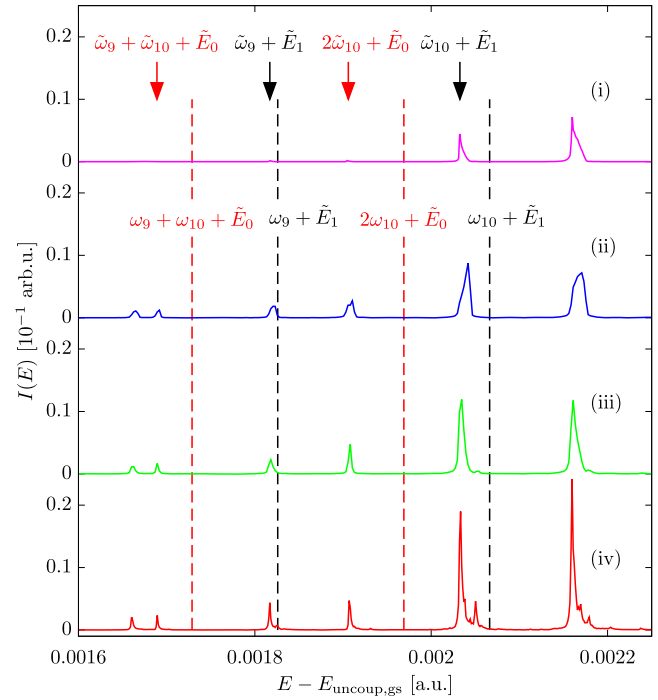


FIG. 2. Bath excitations in the spectrum of a Morse oscillator coupled to a CL bath. The rightmost peak is the second excitation of the system, and the remaining peaks originate from bath modes. All bath parameters and plot specifications are identical to Fig. 1. The arrows highlight bath peaks of first order (fundamental) in black and higher order (overtones) in red; dashed vertical lines show the respective uncoupled counterpart.

excited state of the system. For this peak, the full mixed result with one HK DOF [blue line, (ii)] clearly deviates from the reference spectrum. However, this deviation can be removed by also treating the most strongly coupled bath DOF on the HK level of accuracy [green line, (iii)], which reproduces non-Gaussian distortions of the resonant bath mode. The separable mixed result [magenta line, (iv)], on the other hand, agrees within the frequency resolution with the reference HK spectrum, and it is better converged. All remaining peaks in Fig. 2 are bath excitations, highlighted by red and black arrows. Assuming the bath oscillators are still harmonic, they are the sum of one or more shifted bath frequencies $\tilde{\omega}_i$ and either the elastic peak \tilde{E}_0 or the first system excitation \tilde{E}_1 . The dashed lines have been obtained by adding the original bath frequencies ω_i to \tilde{E}_0 or \tilde{E}_1 , and thus illustrate where these bath peaks would be situated if the frequencies remained unchanged by the dynamics. The rightmost red line, for example, shows the second excited state of the HO with the highest frequency. Each bath peak lies to the left of the corresponding dashed line, indicating a redshift. Higher order bath excitations (red arrows in Fig. 2) are shifted further, as it is expected. As discussed in our first paper on the mixed TA-SCIVR,¹ the separable approximation that leads to Eq. (19) entails a suppression of bath excitations. Consequently, only the first excitation of the highest frequency bath mode shows up significantly in the spectrum. Like the excited states of the Morse oscillator, its position agrees closely with the less approximate results. The other bath excitations are strongly suppressed by the separable mixed method, but they can still be identified reliably upon closer inspection and also turn out to be reproduced faithfully.

Due to its numerical advantages, we will perform exclusively separable mixed calculations in the remainder of this paper, where we investigate the system behavior for different bath characteristics.

B. Frequency shifts for different bath sizes and role of the Caldeira-Leggett counter term

Having established that the separable mixed method offers the same accuracy with respect to peak positions as the full HK treatment for the CL system, we now increase the bath size up to 60 bath HOs. Again, we use a very off-resonant bath on the one hand and one with bath frequencies up to the system frequency on the other hand. In addition, we will analyse the influence of the CL counter term on the outcome of the spectral calculations for our examples. We will undertake a similar investigation as previously performed by Georgievskii and Stuchebrukhov⁸⁷ and therefore look at the CL model in the form of Eq. (20) as well as a Hamiltonian without the counter term,

$$H = \frac{p_s^2}{2m_s} + V_s(s) + \sum_{i=1}^{F_b} \left\{ \frac{p_i^2}{2} + \frac{1}{2} \omega_i^2 y_i^2 + c_i y_i (s - s_{eq}) \right\}. \quad (31)$$

The following numerical investigations will comprise bath sizes of 10, 20, 40, and 60 DOFs such that convergence with respect to the number of bath HOs can be tested. As we are using the separable mixed TA-SCIVR, we can keep the number of trajectories constant at 10^4 for the differently sized baths. With this number of trajectories, all results are converged with respect to peak positions. The number of HK DOFs has been either one or two. Especially for the low-frequency bath, it was sufficient to describe only the Morse oscillator with HK, while in the case of the high bath cutoff, it was helpful to include the resonant bath oscillator into the HK part as well.

1. Example: 20 bath DOFs

An exemplary overview of results for the different bath parameters is given in Figs. 3 and 4 for a bath with 20 DOFs, where again all spectra are normalized such that the respective most intense peak's size is one. To illustrate the shift of the

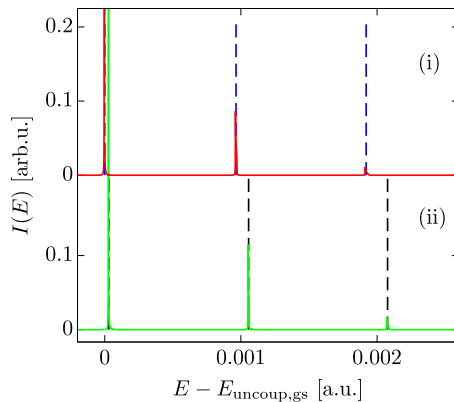


FIG. 3. Spectra for a Morse oscillator in an off-resonant CL bath with 20 HOs. Bath parameters are $\omega_c = 0.1 \omega_s$, $\omega_{\max} = 0.5 \omega_s$, and $\eta_{\text{eff}} = 0.5$. The top result (i) is from a calculation without the CL counter term, and the bottom spectrum (ii) is from a calculation including the CL counter term. The dashed lines represent eigenvalues of a regular 1D Morse potential (blue, top) and of a 1D Morse potential modified by the CL counter term according to Eq. (32) (black, bottom).

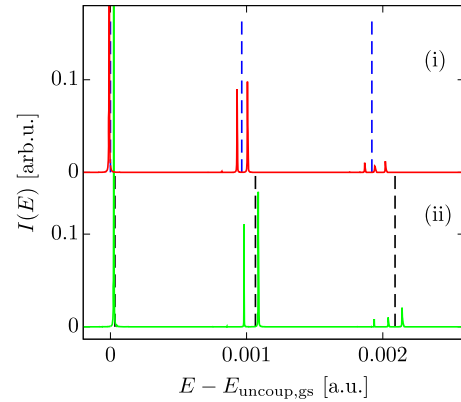


FIG. 4. Spectra for a Morse oscillator in a resonant CL bath with 20 HOs. Bath parameters are $\omega_c = 0.5 \omega_s$, $\omega_{\max} = \omega_s$, and $\eta_{\text{eff}} = 0.5$. All remaining plot specifications as in Fig. 3.

Morse spectrum, we indicate the positions of the analytical eigenvalues of the Morse potential from Eq. (22) for calculations without the CL counter term (top halves of Figs. 3 and 4). For the evaluation of the calculations with the original CL Hamiltonian in Eq. (20), the one-dimensional reference is modified because the counter term, which does not depend on the bath coordinates, effectively amounts to a renormalization of the system potential.⁹⁶ Therefore, in this case we use eigenenergies $E_{\text{mod},n}$ (bottom halves of Figs. 3 and 4) of the Morse potential modified by the CL counter term,

$$V_{s,\text{mod}}(s) = D_e \left(1 - e^{-\alpha(s-s_{eq})} \right)^2 + \frac{\pi F_b}{4a} (s - s_{eq})^2. \quad (32)$$

The spectra with far off-resonant frequencies in Fig. 3 exhibit system peaks that are hardly different from the 1D results on this scale. If the CL counter term is included (bottom half), we see a blueshift that can be attributed to the modification of the system potential by the counter term. Choosing the cutoff frequency closer to ω_s , on the other hand, has a much greater impact on the spectra, as depicted in Fig. 4. Instead of just the excited states of the system, we now see red-shifted bath excitations and a blue-shifted system peak as in Fig. 2. The prominence of these bath peaks is due to the resonant bath mode that can be driven much more effectively by the system than the non-resonant one from the low-cutoff example. In addition, the resonant HO is now incorporated into the HK part of the calculation, which does not suppress bath overtones. The more interesting and more relevant feature for us, however, is that the stronger system-bath interaction results in a sizable blueshift of the system both for calculations with and without the CL counter term and always relative to the respective modified or unmodified one-dimensional eigenvalues. For both resonant bath and off-resonant bath, increasing the effective coupling η_{eff} leads to an enhancement of the respective trend towards blueshift or redshift but has no influence on the quality of the shift.

2. Dependence on bath size and CL counter term

For a more detailed quantitative discussion of the system's blueshift, we take a look at the first five system peaks for each of the different baths (Figs. 5–8). In Figs. 5 and 7, the shift of the peak energies is plotted. In a similar way as before, the

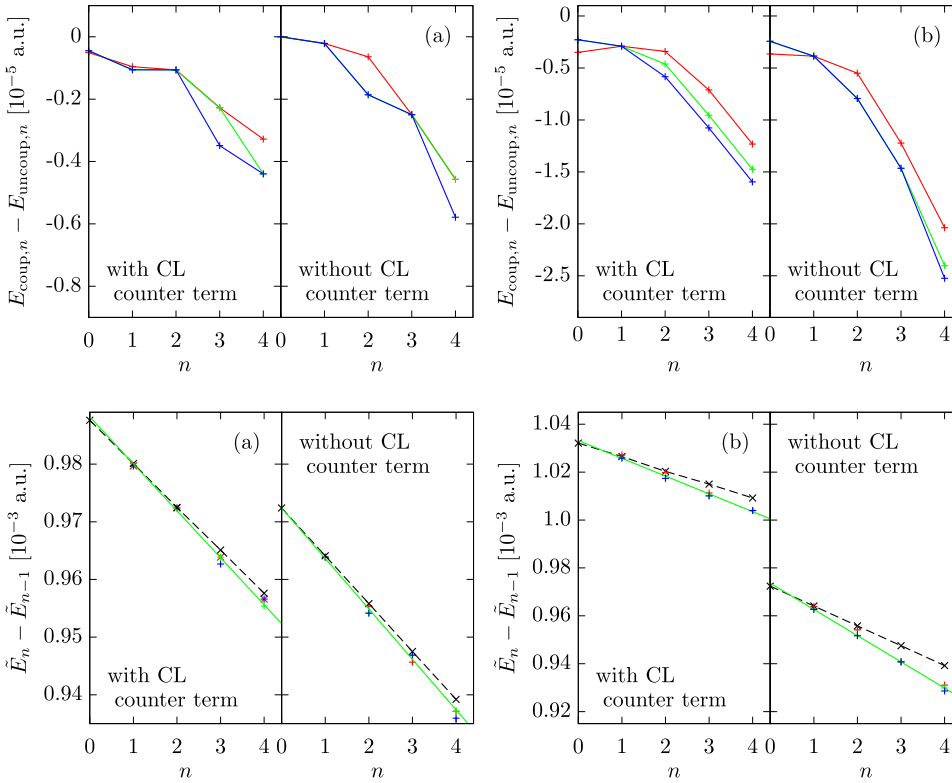


FIG. 5. Shift of the eigenenergies [Eq. (33)] of a Morse oscillator coupled to an off-resonant CL bath with parameters $\omega_{\max} = 0.5 \omega_s$, $\omega_c = 0.1 \omega_s$. The coupling strength is $\eta_{\text{eff}} = 0.5$ in (a) and $\eta_{\text{eff}} = 2.0$ in (b). The bath comprises either 10 (red crosses), 20 (green crosses), or 40 (blue crosses) HO, and the solid lines are just a guide to the eye. The CL counter term is included in the calculations on the left side of each panel and not included on the right side [Eq. (31)].

energy of an appropriate uncoupled reference, now depending on the peak index, is subtracted,

$$E_{\text{plot},n} = E_{\text{coup},n} - \left(E_{s,n} + \sum_{i=1}^{F_b} \frac{\omega_i}{2} \right), \quad (33)$$

where the system eigenenergies $E_{s,n}$ are either the analytic eigenenergies E_n of the undisturbed Morse potential from Eq. (21) for the calculations without the CL counter term or the numerically calculated eigenenergies $E_{\text{mod},n}$ of the modified Morse potential from Eq. (32) for the calculations including the counter term. Thus, we visualize the net shift of the peaks, which includes the energy shifts of the system eigenstates and of the bath ground state. A blueshift of the system is characterized by a sequence of increasing values, whereas a redshift shows the opposite behavior. Assuming that the interaction with the bath only changes the Morse parameters of the system to $\tilde{\omega}_e$ and \tilde{x}_e , but not the overall Morse form itself, Eq. (33) has the form of a parabola, as can be seen by inserting the Morse

eigenvalues from Eq. (22),

$$E_{\text{plot},n} = (\tilde{\omega}_e - \omega_e) \left(n + \frac{1}{2} \right) - (\tilde{\omega}_e \tilde{x}_e - \omega_e x_e) \left(n + \frac{1}{2} \right)^2 - \Delta E_{\text{b,gs}}. \quad (34)$$

The last term in this equation is the change of the bath ground state energy upon coupling to the system, which acts as a constant offset.

As an alternative measure, Figs. 6 and 8 show the difference of consecutive excited Morse peaks, $\tilde{E}_n - \tilde{E}_{n-1}$, such that the shift of the bath ground state energy $\Delta E_{\text{b,gs}}$ drops out. This kind of representation is referred to as the Birge-Sponer extrapolation and can be used experimentally to determine Morse potential parameters from spectroscopic data.⁹⁷ Based on the analytic formula for the Morse eigenenergies in Eq. (22), a linear fit of these points yields the harmonic approximation frequency ω_e as the intersection with the vertical axis and the

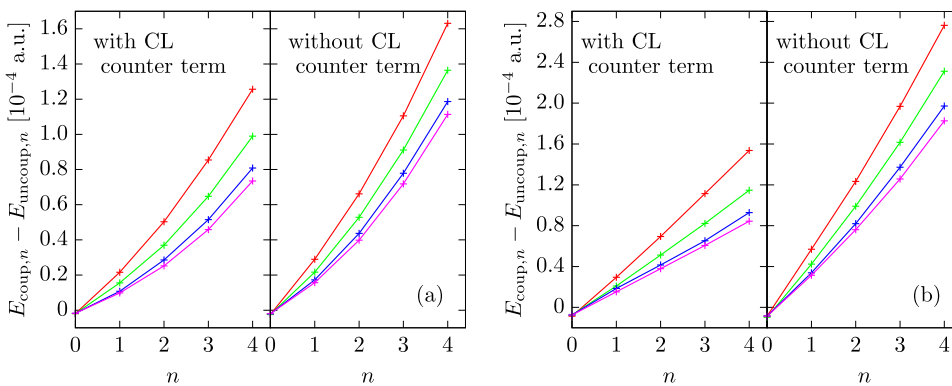


FIG. 7. Shift of the eigenenergies of a MO coupled to a resonant CL bath with parameters $\omega_{\max} = \omega_s$, $\omega_c = 0.5 \omega_s$, and coupling strengths $\eta_{\text{eff}} = 0.1$ in (a) and $\eta_{\text{eff}} = 0.5$ in (b). All plot specifications as in Fig. 5, with the addition of results for 60 bath DOFs (magenta crosses).

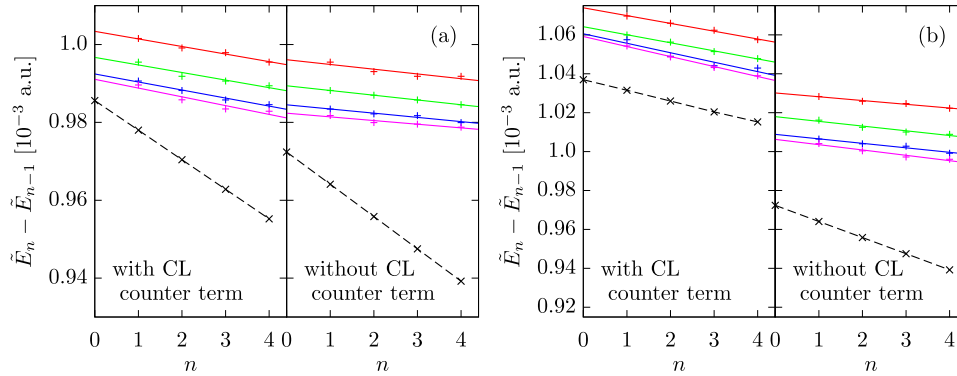


FIG. 8. Birge-Sponer fit to the difference of consecutive eigenenergies \tilde{E}_n of a Morse oscillator coupled to the resonant CL bath from Fig. 7. All lines are fits to points of the same color as in Fig. 6, with the color code from Fig. 7.

anharmonicity $\omega_e x_e$, which is proportional to the slope of the line. An increase of the slope corresponds to a redshift, whereas a decreasing slope means a bigger difference between eigenvalues and therefore a blueshift. We show a linear fit of the first four system energy differences and compare this result to the one-dimensional Morse oscillator or its modified version (black “x,” dashed line), for which ω_e has also been obtained by the Birge-Sponer fit and is indicated with an “x.” The shifts of the experimental parameters with respect to the gas-phase result are summarized in Table I.

a. Off-resonant bath. The analysis is interesting especially for the low-frequency bath, where we could not see much in the overview plot (Fig. 4). Results are presented in Figs. 5 and 6. Due to the fits in the Birge-Sponer plots in Fig. 6 being almost identical, we have plotted only one line in each case. For low coupling, we see an almost negligible redshift. The effect of the CL counter term is well illustrated by the Birge-Sponer plot: the result with the counter term is clearly blueshifted with respect to the original Morse eigenvalues, but it is almost on top of the appropriately modified 1D energies. The influence of the system-bath dynamics is much smaller by comparison, especially given that our energy grid resolution is $\Delta E = 1.2 \times 10^{-6}$ a.u. These findings are corroborated by the calculations with higher system-bath coupling strength. Here, the redshift is much more pronounced, but again, for the original CL potential, the main contribution to the energy shift is due to the counter term. For all calculations with low bath cutoff frequency, the number of bath oscillators does not have much impact on the system spectrum. In the low coupling case, the difference between all three bath sizes is one frequency grid point at most. For the higher coupling, 10 bath DOFs influence the system somewhat less than 20 and 40 bath HOs, which yield very similar results. This weak dependence on

bath size is a consequence of the low cutoff and maximum bath frequencies. While the bath mode with the highest frequency is always the same, most additional bath oscillators are far off-resonant. In conclusion, we find the same 20 to 40 bath DOFs to be sufficient to describe a continuous low-frequency bath, as it has been reported in Ref. 20.

b. Resonant bath. The case of baths with a high cutoff and resonant maximum frequency is investigated in detail in Figs. 7 and 8. The overall behavior of the system is completely different compared to the low-frequency case, with strong blueshifts for each bath setup, as already seen in the overview, Fig. 4. For $\eta_{\text{eff}} = 0.1$, the effect of the bath on the system is somewhat bigger without the CL counter term, as shown on the left side of Fig. 7(a). The counter term, which is harmonic in the system coordinate, restricts the system dynamics and thus also the system-bath interaction. If it is left out of the calculation, the system-bath dynamics induces a larger shift of the system frequency. The total blueshift in Fig. 8, on the other hand, is also determined by the change of the 1D eigenenergies by the counter term, which offsets the weaker system-bath dynamics and leads to quite similar overall results in this low-coupling case. Unlike before, the results strongly depend on the bath size because each increase adds in particular some oscillators that are close to the system frequency and notably influence the system’s dynamics. As the differences between results become smaller with each addition of bath HOs, we approach convergence with respect to a continuous bath description with 60 bath DOFs. The higher system-bath coupling amplifies these trends. Now, the difference of coupled and uncoupled peak energies [Fig. 7(b)] is almost twice as big for the calculation without the CL counter term compared to the one that includes it. However, the modification of the 1D eigenenergies induced by the counter term is so big in this case that the total blueshift [Fig. 8(b)] becomes even larger than without the counter term. Again, we can see that the results converge with increasing bath size.

3. Frequency shift dependence on cutoff and maximum frequency

Given the different nature of the system frequency shift in Figs. 5 and 7, one may wonder how the transition from redshift to blueshift looks like for varying bath cutoff or maximum frequency. This is illustrated exemplarily in Figs. 9 and 10 for a bath with 20 HOs and using the Hamiltonian without the CL counter term. In Fig. 9, we keep the maximum frequency fixed,

TABLE I. Change of the harmonic frequency and the anharmonicity of a Morse oscillator in the presence of a Caldeira-Leggett bath. All shifts are relative to the gas-phase result.

	Resonant bath	Off-resonant bath
With CL counter term (Eq. (20))	$\tilde{\omega}_e > \omega_e$ $\tilde{\omega}_e x_e < \omega_e x_e$	$\tilde{\omega}_e > \omega_e$ $\tilde{\omega}_e x_e < \omega_e x_e$
Without CL counter term (Eq. (31))	$\tilde{\omega}_e > \omega_e$ $\tilde{\omega}_e x_e > \omega_e x_e$	$\tilde{\omega}_e > \omega_e$ $\tilde{\omega}_e x_e < \omega_e x_e$

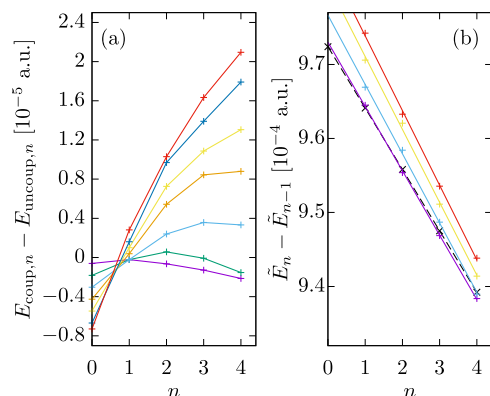


FIG. 9. Cutoff frequency dependence of the shift of the eigenenergies of a Morse oscillator coupled to a CL bath. Bath parameters: 20 HOs, maximum frequency fixed at $\omega_{\max} = 0.7 \omega_s$, and cutoff frequencies ω_c are $0.1 \omega_s$ (violet “+” crosses), $0.2 \omega_s$ (green), $0.3 \omega_s$ (light blue), $0.4 \omega_s$ (orange), $0.5 \omega_s$ (yellow), $0.6 \omega_s$ (dark blue), and $0.7 \omega_s$ (red). The CL counter term is not included in the Hamiltonian [Eq. (31)]. The “x” crosses and black dashed line show the eigenenergy differences of the gas-phase Morse oscillator. The lines in (a) are just a guide to the eye. In (b), the lines are the linear fit to the crosses of the same color.

while the cutoff frequency is varied. As expected from the above investigations, the blueshift of the higher eigenfrequencies is gradually diminished and finally turns into a redshift as the bath oscillators become more off-resonant. Taking the parabola from Eq. (34) as an appropriate description for the curves in Fig. 9(a), we see that indeed all of these graphs display a negative curvature, which is equivalent to an increase and therefore a redshift of the anharmonicity $\tilde{\omega}_e \tilde{x}_e$. This is corroborated by the Birge-Sponer plot in Fig. 9(b), where it shows a steeper slope of the linear fit. The harmonic approximation frequency $\tilde{\omega}_e$ is always blue-shifted, and the shift is enhanced as ω_c grows.

A similar behavior is observed for the opposite case displayed in Fig. 10, where we keep the cutoff frequency fixed and vary the maximum frequency. There is a change from redshift to blueshift of the anharmonicity as the maximum

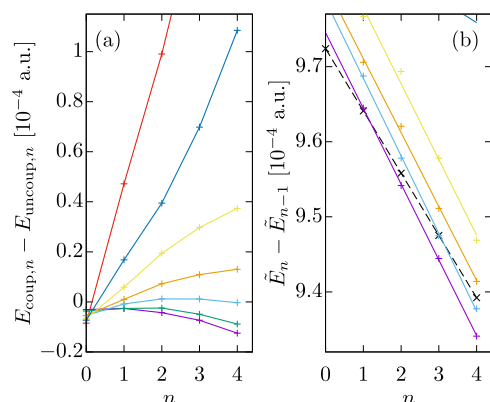


FIG. 10. Maximum bath frequency dependence of the shift of the eigenenergies of a Morse oscillator coupled to a CL bath. Bath parameters: 20 HOs, cutoff frequency fixed at $\omega_c = 0.5 \omega_s$, and maximum frequencies ω_{\max} are $0.4 \omega_s$ (violet “+” crosses), $0.5 \omega_s$ (green), $0.6 \omega_s$ (light blue), $0.7 \omega_s$ (orange), $0.8 \omega_s$ (yellow), $0.9 \omega_s$ (dark blue), and $1.0 \omega_s$ (red). The CL counter term is not included in the Hamiltonian [Eq. (31)]. The “x” crosses and black dashed line show the eigenenergy differences of the gas-phase Morse oscillator. The lines in (a) are just a guide to the eye. In (b), the lines are the linear fit to the crosses of the same color.

bath frequency becomes resonant and more close-to-resonant modes are present in the bath, as already seen in Figs. 7 and 8. As the maximum frequency becomes more off-resonant, we again see a redshift of the anharmonicity. In both cases, the harmonic frequency is shifted to a higher value.

V. CONCLUSIONS AND OUTLOOK

The spectral lines of an anharmonic system of interest are strongly influenced by the presence of coupling to an environment. In an energy domain Green’s function calculation, the self-energy due to the environmental coupling leads to a shift (and broadening) of the peaks.⁸⁷ Here, we use an alternative, time-dependent methodology and investigate the influence on the spectroscopic signatures of large environments with up to 60 bath degrees of freedom that are treated explicitly together with the system. Conditions on the bath parameters have been identified that lead either to a redshift or to a blueshift of the system frequency. We have investigated the cases of a non-resonant bath and a resonant bath, where in the latter case also the bath oscillator closest to resonance was treated at the HK level. Furthermore, we have compared results from calculations with and without the Caldeira-Leggett counter term to demonstrate that this term causes a large portion of the blueshift which is observed with respect to the gas-phase Morse oscillator. If the one-dimensional reference potential is adjusted appropriately with the counter term, the effect of the system-bath interaction on the system eigenenergies is similar for calculations with and without the counter term. The change of the system frequency depends on both the bath cutoff and the maximum frequency. In the case of a strongly non-resonant bath, the anharmonicity $\omega_e x_e$ is red-shifted. The harmonic frequency ω_e always shifts to a higher value. If there are at least some bath frequencies close to resonance, on the other hand, the fundamental frequency and the anharmonicity are blue-shifted. Overall, the mixed time averaged semiclassical hybrid approach demonstrated to be a robust semiclassical approximation that properly accounts for different types of coupling, even for up to 61-dimensional potential. This opens the route of its application to more realistic condensed phase systems than the Caldeira-Leggett potential modeling.

Recently, it has been argued that the modeling of an anharmonic system bilinearly coupled to a harmonic bath suffers the invertibility problem.⁹⁸ The next goal that we intend to tackle therefore is the study of realistic system-bath Hamiltonians with Lennard-Jones type interaction, for systems like iodine in a Krypton matrix, which have also been studied experimentally.⁸⁵

Future implementation will include the finite temperature effects and the broadening of the peaks. Eventually, given the cheap computational cost of the time-averaging SC-IVR, the present mixed semiclassical method will be implemented for direct *ab initio* simulations of condensed phase systems.

ACKNOWLEDGMENTS

Michele Ceotto and Max Buchholz acknowledge financial support from the European Research Council (ERC) under the European Union’s Horizon 2020 research and

innovation programme [Grant Agreement No. (647107)—SEMICOMPLEX—ERC-2014-CoG]. M.C. also acknowledges the CINECA and the Regione Lombardia award under the LISA initiative (Grant No. GREENTI) for the availability of high performance computing resources. M.B. acknowledges funding from the Graduate Academy of TU Dresden as well as from the IMPRS of the MPI-PKS Dresden.

- ¹M. Buchholz, F. Grossmann, and M. Ceotto, *J. Chem. Phys.* **144**, 094102 (2016).
- ²Y. Elran and K. G. Kay, *J. Chem. Phys.* **110**, 3653 (1999).
- ³A. L. Kaledin and W. H. Miller, *J. Chem. Phys.* **118**, 7174 (2003).
- ⁴F. Grossmann, *J. Chem. Phys.* **125**, 014111 (2006).
- ⁵E. J. Heller, *Acc. Chem. Res.* **14**, 368 (1981).
- ⁶W. H. Miller, *J. Chem. Phys.* **53**, 3578 (1970).
- ⁷E. J. Heller, *J. Chem. Phys.* **62**, 1544 (1975).
- ⁸S. Levit and U. Smilansky, *Ann. Phys.* **103**, 198 (1977).
- ⁹E. J. Heller, *J. Chem. Phys.* **75**, 2923 (1981).
- ¹⁰M. F. Herman and E. Kluk, *Chem. Phys.* **91**, 27 (1984).
- ¹¹E. J. Heller, in *Chaos et Physique Quantique/Chaos and Quantum Physics*, Proceedings of the Les Houches Summer School, Session LII 1989, edited by M. J. Giannoni, A. Voros, and J. Zinn-Justin (North-Holland, Amsterdam, 1991).
- ¹²W. H. Miller, *J. Phys. Chem. A* **105**, 2942 (2001).
- ¹³K. G. Kay, *J. Chem. Phys.* **100**, 4377 (1994).
- ¹⁴K. G. Kay, *J. Chem. Phys.* **100**, 4432 (1994).
- ¹⁵K. G. Kay, *J. Chem. Phys.* **101**, 2250 (1994).
- ¹⁶F. Grossmann and A. L. Xavier, Jr., *Phys. Lett. A* **243**, 243 (1998).
- ¹⁷W. H. Miller, *J. Phys. Chem. A* **102**, 793 (1998).
- ¹⁸X. Sun and W. H. Miller, *J. Chem. Phys.* **110**, 6635 (1999).
- ¹⁹M. Thoss, H. Wang, and W. H. Miller, *J. Chem. Phys.* **115**, 2991 (2001).
- ²⁰H. Wang, M. Thoss, K. L. Sørge, R. Gelabert, X. Giménez, and W. H. Miller, *J. Chem. Phys.* **114**, 2562 (2001).
- ²¹H. Wang, M. Thoss, and W. H. Miller, *J. Chem. Phys.* **112**, 47 (2000).
- ²²R. Gelabert, X. Giménez, M. Thoss, H. Wang, and W. H. Miller, *J. Chem. Phys.* **114**, 2572 (2001).
- ²³T. Yamamoto, H. Wang, and W. H. Miller, *J. Chem. Phys.* **116**, 7335 (2002).
- ²⁴W. H. Miller, *Proc. Natl. Acad. Sci. U. S. A.* **102**, 6660 (2005).
- ²⁵J. Liu and W. H. Miller, *J. Chem. Phys.* **126**, 234110 (2007).
- ²⁶J. Liu and W. H. Miller, *J. Chem. Phys.* **127**, 114506 (2007).
- ²⁷G. Tao and W. H. Miller, *J. Chem. Phys.* **135**, 024104 (2011).
- ²⁸W. H. Miller, *J. Chem. Phys.* **125**, 132305 (2006).
- ²⁹D. V. Shalashilin and M. S. Child, *Chem. Phys.* **304**, 103 (2004).
- ³⁰K. G. Kay, *Chem. Phys.* **322**, 3 (2006).
- ³¹T. Sklarz and K. G. Kay, *J. Chem. Phys.* **120**, 2606 (2004).
- ³²C. Harabati and K. G. Kay, *J. Chem. Phys.* **127**, 084104 (2007).
- ³³G. Hochman and K. G. Kay, *J. Chem. Phys.* **130**, 061104 (2009).
- ³⁴M. F. Herman, *Annu. Rev. Phys. Chem.* **45**, 83 (1994).
- ³⁵N. Makri, *Annu. Rev. Phys. Chem.* **50**, 167 (1999).
- ³⁶S. Zhang and E. Pollak, *J. Chem. Phys.* **121**, 3384 (2004).
- ³⁷S. Zhang and E. Pollak, *J. Chem. Theory Comput.* **1**, 345 (2005).
- ³⁸J. Shao and E. Pollak, *J. Chem. Phys.* **125**, 133502 (2006).
- ³⁹E. Pollak and E. Martin-Fierro, *J. Chem. Phys.* **126**, 164107 (2007).
- ⁴⁰E. Martin-Fierro and E. Pollak, *J. Chem. Phys.* **125**, 164104 (2006).
- ⁴¹A. R. Walton and D. E. Manolopoulos, *Chem. Phys. Lett.* **244**, 448 (1995).
- ⁴²A. R. Walton and D. E. Manolopoulos, *Mol. Phys.* **87**, 961 (1996).
- ⁴³M. L. Brewer, J. S. Hulme, and D. E. Manolopoulos, *J. Chem. Phys.* **106**, 4832 (1997).
- ⁴⁴S. Bonella and D. F. Coker, *J. Chem. Phys.* **118**, 4370 (2003).
- ⁴⁵S. Bonella, D. Montemayor, and D. F. Coker, *Proc. Natl. Acad. Sci. U. S. A.* **102**, 6715 (2005).
- ⁴⁶C. Harabati, J. M. Rost, and F. Grossmann, *J. Chem. Phys.* **120**, 26 (2004).
- ⁴⁷F. Grossmann, *Comments At. Mol. Phys.* **34**, 141 (1999).
- ⁴⁸T. F. Viscondi and M. A. M. de Aguiar, *J. Chem. Phys.* **134**, 234105 (2011).
- ⁴⁹S. V. Antipov, Z. Ye, and N. Ananth, *J. Chem. Phys.* **142**, 184102 (2015).
- ⁵⁰C. Venkataraman, *J. Chem. Phys.* **135**, 204503 (2011).
- ⁵¹H. Nakamura, S. Nanbu, Y. Teranishic, and A. Ohtab, *Phys. Chem. Chem. Phys.* **18**, 11972 (2016).
- ⁵²A. D. Kondorskiy and S. Nanbu, *J. Chem. Phys.* **143**, 114103 (2015).
- ⁵³J. Tatchen and E. Pollak, *J. Chem. Phys.* **130**, 041103 (2009).
- ⁵⁴P. Huo and D. F. Coker, *J. Chem. Phys.* **135**, 201101 (2011).
- ⁵⁵M. S. Church, S. V. Antipov, and N. Ananth, *J. Chem. Phys.* **146**, 234104 (2017).
- ⁵⁶M. Ceotto, S. Atahan, G. F. Tantardini, and A. Aspuru-Guzik, *J. Chem. Phys.* **130**, 234113 (2009).
- ⁵⁷M. Ceotto, S. Atahan, S. Shim, G. F. Tantardini, and A. Aspuru-Guzik, *Phys. Chem. Chem. Phys.* **11**, 3861 (2009).
- ⁵⁸M. Ceotto, G. F. Tantardini, and A. Aspuru-Guzik, *J. Chem. Phys.* **135**, 214108 (2011).
- ⁵⁹M. Ceotto, Y. Zhuang, and W. L. Hase, *J. Chem. Phys.* **138**, 054116 (2013).
- ⁶⁰R. Conte, A. Aspuru-Guzik, and M. Ceotto, *J. Phys. Chem. Lett.* **4**, 3407 (2013).
- ⁶¹R. Ianculescu, J. Tatchen, and E. Pollak, *J. Chem. Phys.* **139**, 154311 (2013).
- ⁶²S. Y. Y. Wong, D. M. Benoit, M. Lewerenz, A. Brown, and P.-N. Roy, *J. Chem. Phys.* **134**, 094110 (2011).
- ⁶³M. Wehrle, M. Šulc, and J. Vaníček, *J. Chem. Phys.* **140**, 244114 (2014).
- ⁶⁴M. Wehrle, S. Oberli, and J. Vaníček, *J. Phys. Chem. A* **119**, 5685 (2015).
- ⁶⁵T. Zimmermann and J. Vaníček, *J. Chem. Phys.* **137**, 22A516 (2012).
- ⁶⁶T. Zimmermann and J. Vaníček, *J. Chem. Phys.* **141**, 134102 (2014).
- ⁶⁷A. L. Kaledin and W. H. Miller, *J. Chem. Phys.* **119**, 3078 (2003).
- ⁶⁸G. Di Liberto and M. Ceotto, *J. Chem. Phys.* **145**, 144107 (2016).
- ⁶⁹D. Tamascelli, F. S. Dambrosio, R. Conte, and M. Ceotto, *J. Chem. Phys.* **140**, 174109 (2014).
- ⁷⁰F. Gabas, R. Conte, and M. Ceotto, *J. Chem. Theory Comput.* **13**, 2378 (2017).
- ⁷¹M. Ceotto, S. Valleau, G. F. Tantardini, and A. Aspuru-Guzik, *J. Chem. Phys.* **134**, 234103 (2011).
- ⁷²M. Ceotto, D. dell'Angelo, and G. F. Tantardini, *J. Chem. Phys.* **133**, 054701 (2010).
- ⁷³M. Ceotto, G. D. Liberto, and R. Conte, *Phys. Rev. Lett.* **119**, 010401 (2017).
- ⁷⁴A. O. Caldeira and A. J. Leggett, *Phys. Rev. Lett.* **46**, 211 (1981).
- ⁷⁵E. Pollak, *Phys. Rev. A* **33**, 4244 (1986).
- ⁷⁶F. Grossmann, *J. Chem. Phys.* **103**, 3696 (1995).
- ⁷⁷J. Cao, *J. Chem. Phys.* **107**, 3204 (1997).
- ⁷⁸U. Weiss, *Quantum Dissipative Systems* (World Scientific, 1999).
- ⁷⁹Y. Tanimura, *J. Phys. Soc. Jpn.* **75**, 082001 (2006).
- ⁸⁰M. Bonfanti, G. F. Tantardini, K. H. Hughes, R. Martinazzo, and I. Burghardt, *J. Phys. Chem. A* **116**, 11406 (2012).
- ⁸¹S. Garashchuk, V. Dixit, B. Gu, and J. Mazzuca, *J. Chem. Phys.* **138**, 054107 (2013).
- ⁸²A. M. Levine, M. Shapiro, and E. Pollak, *J. Chem. Phys.* **88**, 1959 (1988).
- ⁸³R. B. Williams and R. F. Loring, *J. Chem. Phys.* **110**, 10899 (1999).
- ⁸⁴T. Joutsuka and K. Ando, *J. Chem. Phys.* **134**, 204511 (2011).
- ⁸⁵M. Karavitis, R. Zadoyan, and V. A. Apkarian, *J. Chem. Phys.* **114**, 4131 (2001).
- ⁸⁶M. Karavitis and V. A. Apkarian, *J. Chem. Phys.* **120**, 292 (2004).
- ⁸⁷Y. I. Georgievskii and A. A. Stuchebrukhov, *J. Chem. Phys.* **93**, 6699 (1990).
- ⁸⁸Y. Zhuang, M. R. Siebert, W. L. Hase, K. G. Kay, and M. Ceotto, *J. Chem. Theory Comput.* **9**, 54 (2013).
- ⁸⁹L. Bonnet, *J. Chem. Phys.* **139**, 114108 (2013).
- ⁹⁰J. Liu, *Int. J. Quantum Chem.* **115**, 657 (2015).
- ⁹¹J. Liu, W. H. Miller, G. S. Fanourgakis, S. S. Xantheas, S. Imoto, and S. Saito, *J. Chem. Phys.* **135**, 244503 (2011).
- ⁹²M. Ovchinnikov and V. A. Apkarian, *J. Chem. Phys.* **105**, 10312 (1996).
- ⁹³G.-L. Ingold, in *Coherent Evolution in Noisy Environments*, Lecture Notes in Physics, edited by A. Buchleitner and K. Hornberger (Springer-Verlag, Berlin, Heidelberg, 2002), Vol. 611, Chap. 1, pp. 1–53.
- ⁹⁴C.-M. Goletz and F. Grossmann, *J. Chem. Phys.* **130**, 244107 (2009).
- ⁹⁵C.-M. Goletz, W. Koch, and F. Grossmann, *Chem. Phys.* **375**, 227 (2010).
- ⁹⁶M. Rosenau da Costa, A. O. Caldeira, S. M. Dutra, and H. Westfahl, *Phys. Rev. A* **61**, 022107 (2000).
- ⁹⁷E. L. Lewis, C. W. P. Palmer, and J. L. Cruickshank, *Am. J. Phys.* **62**, 350 (1994).
- ⁹⁸F. Gottwald, S. D. Ivanov, and O. Kühn, *J. Phys. Chem. Lett.* **6**, 2722 (2015).